such as the slow slip observed just before the Tohoku-Oki earthquake (*29*). Therefore, monitoring the spatiotemporal changes of shallow slow earthquakes is important for evaluating the slip of the shallow plate interface offshore. This aids assessment of the potential hazard of tsunamigenic earthquakes. Long-term ocean-bottom observations of many subduction zones and geodetic observations to confirm the suspected shallow SSEs for this region will further clarify the relationship between shallow slow earthquakes and the frictional behavior of megathrusts.

REFERENCES AND NOTES

1. K. Obara, *Science* **296**, 1679–1681 (2002).
2. G. Dragert, K. Wang, T. S. James, *Science* **292**, 1525–1528 (2001).
3. G. Rogers, H. Dragert, *Science* **300**, 1942–1943 (2003).
4. K. Obara, H. Hirose, F. Yamamizu, K. Kasahara, *Geophys. Res. Lett.* **31**, L23602 (2004).
5. Y. Ito, K. Obara, K. Shiomi, S. Sekine, H. Hirose, *Science* **315**, 503–506 (2007).
6. S. Ide, D. Shelly, G. Beroza, *Geophys. Res. Lett.* **34**, L03308 (2007).
7. K. Obara, T. Matsuzawa, S. Tanaka, T. Kimura, T. Maeda, *Geophys. Res. Lett.* **38**, L09311 (2011).
8. C. H. Scholz, J. Campos, *J. Geophys. Res.* **117**, B05310 (2012).
9. K. Obara, Y. Ito, *Earth Planets Space* **57**, 321–326 (2005).
10. Y. Asano, K. Obara, Y. Ito, *Earth Planets Space* **60**, 871–875 (2008).
11. H. Sugioka *et al.*, *Nat. Geosci.* **5**, 414–418 (2012).
12. J. I. Walter, S. Y. Schwartz, M. Protti, V. Gonzalez, *Geophys. Res. Lett.* **40**, 1517–1522 (2013).
13. K. Obana, S. Kodaira, *Earth Planet. Sci. Lett.* **287**, 168–174 (2009).
14. T. Nishimura, *Prog. Earth Planet. Sci.* **1**, 22 (2014).
15. L. M. Wallace *et al.*, *Geology* **37**, 143–146 (2009).
16. Y. Yamashita, H. Shimizu, K. Goto, *Geophys. Res. Lett.* **39**, L08304 (2012).
17. Materials and methods are available as supplementary materials on *Science* Online.
18. K. Obara, *J. Geophys. Res.* **115**, B00A25 (2010).
19. H. Houston, B. G. Delbridge, A. G. Wech, K. C. Creager, *Nat. Geosci.* **4**, 404–409 (2011).
20. H. Dragert, K. Wang, *J. Geophys. Res.* **116**, B12406 (2011).
21. R. Ando, R. Nakata, T. Hori, *Geophys. Res. Lett.* **37**, L10310 (2010).
22. N. M. Bartlow, S. Miyazaki, A. M. Bradley, P. Segall, *Geophys. Res. Lett.* **38**, L18309 (2011).
23. A. Ghosh *et al.*, *Geochem. Geophys. Geosyst.* **11**, Q12010 (2010).
24. Y. Yamamoto *et al.*, *Tectonophysics* **589**, 90–102 (2013).
25. K. Wang, S. L. Bilek, *Geology* **39**, 819–822 (2011).
26. Y. Yagi, M. Kikuchi, S. Yoshida, Y. Yamanaka, *J. Seismol. Soc. Jpn.* **2**, 139–148 (1998).
27. Y. Yagi, M. Kikuchi, S. Yoshida, T. Sagiya, *Geophys. Res. Lett.* **26**, 3161–3164 (1999).
28. T. Matsuzawa, H. Hirose, B. Shibazaki, K. Obara, *J. Geophys. Res.* **115**, B12301 (2010).
29. A. Kato *et al.*, *Science* **335**, 705–708 (2012).
30. S. Miyazaki, K. Heki, *J. Geophys. Res.* **106**, 4305–4326 (2001).

ACKNOWLEDGMENTS

We thank the crew of the *T/S Nagasaki-maru* (Faculty of Fisheries, Nagasaki University) for their skillful work and K. Creager, H. Houston, M. Vallee, K. Goto, Y. Yamanaka, K. Mochizuki, the members of SEVO of Kyushu University, and the ERI of The University of Tokyo for valuable discussions and comments. We also thank the anonymous reviewers for providing suggestions and comments that improved the manuscript. This study was supported by the Ministry of Education, Culture, Sports, Science and Technology (MEXT) of Japan under its Observation and Research Program for Prediction of Earthquakes and Volcanic Eruptions. Y.Y. received support as a Japan Society for the Promotion of Science research fellow (grant 24-3726). Shallow tremor catalog data are available in the supplementary materials.

SUPPLEMENTARY MATERIALS

www.sciencemag.org/content/348/6235/676/suppl/DC1
Materials and Methods
Figs. S1 to S9
References (*31*–*35*)
Data S1

8 December 2014; accepted 30 March 2015
10.1126/science.aaa4242

SURFACE SCIENCE

Adhesion and friction in mesoscopic graphite contacts

Elad Koren, Emanuel Lörtscher, Colin Rawlings, Armin W. Knoll, Urs Duerig*

The weak interlayer binding in two-dimensional layered materials such as graphite gives rise to poorly understood low-friction characteristics. Accurate measurements of the adhesion forces governing the overall mechanical stability have also remained elusive. We report on the direct mechanical measurement of line tension and friction forces acting in sheared mesoscale graphite structures. We show that the friction is fundamentally stochastic in nature and is attributable to the interaction between the incommensurate interface lattices. We also measured an adhesion energy of 0.227 ± 0.005 joules per square meter, in excellent agreement with theoretical models. In addition, bistable all-mechanical memory cell structures and rotational bearings have been realized by exploiting position locking, which is provided solely by the adhesion energy.

Adhesion and friction play a central role in mechanical systems because they are directly responsible for the energetics, dissipation, and wear (*1*). In particular, nanoscale systems are exceptionally susceptible to adhesion and friction as a consequence of a very large surface-to-volume ratio (*2*). Motivated by these issues, research has strongly focused on layered materials exhibiting weak layer-to-layer coupling, henceforth referred to as interlayer binding. Carbon-based materials are a particularly promising material class in this respect. A general phenomenon associated with layered materials is the strong suppression of sliding friction and stiction forces, termed superlubricity (*3*–*5*). Superlubricity arises from a structural mismatch between rotated atomically flat surfaces. As a result, shear displacements in mesoscale structures that are cut along a glide plane spontaneously revert to the initial equilibrium position, solely driven by interfacial adhesion forces, as soon as the externally applied displacement force is released (*6*, *7*).

In view of the high prospective impact of graphitic materials, many research groups have studied the interlayer binding energy theoretically. However, such calculations are challenging because of the substantial contribution from van der Waals interactions and the localized nature of the π-orbital bonding across the graphite planes (*8*–*12*). Current estimates for the interlayer binding energy range from 0.14 J m^{-2} (24 meV per atom) to 0.34 J m^{-2} (56 meV per atom). Experimental data for the adhesion energy of graphite are scarce, and measurements rely on indirect methods building on the exfoliation of multiwalled carbon nanotubes, $\sigma = 0.21 \pm 0.06$ J m^{-2} (*13*); the flexure mechanics of thin graphite sheets, $\sigma = 0.19 \pm 0.01$ J m^{-2} (*14*); or measurements of the desorption energy of aromatic molecules, $\sigma = 0.32 \pm 0.03$ J m^{-2} (*15*). We distinguish between the theoretically calculated binding energy (pertaining to the separation of two surfaces that initially are in perfect atomic registry) and the experimental adhesion energy (relating to the separation of two surfaces from an equilibrium contact position for which the lattices do not necessarily match).

Adhesion and friction in layered materials in general, and in graphite specifically, are not well understood. Here, we report on an experimental study of the interface adhesion and friction in mesoscopic structures made of highly oriented pyrolytic graphite (HOPG). We exploit the unique nanopositioning accuracy and force sensitivity of scanning probe microscopy to repeatedly shear individual nano-sized graphitic mesa structures and to measure the applied shear forces during their mechanical exfoliation along a single basal glide plane. The shear force is composed of a reversible displacement force and a smaller irreversible friction force characterized by a force hysteresis. This strategy allows us to investigate the fundamental mechanisms leading to friction and to relate the reversible displacement force to the adhesion interaction between the sliding surfaces. In addition, the displacement force characteristics can be engineered by the mesa design outline to yield multiple local energy minima at which the sheared structures can be arrested.

The studies were performed on an atomic force microscopy (AFM) setup under ambient conditions. Samples featuring cylindrical and more complex shaped mesa structures with a typical height of 50 nm were fabricated from high-quality HOPG substrates by means of reactive ion etching, using structured Pd-Au metal layers as self-aligned shadow masks (Fig. 1A) (*7*, *14*). For mechanical shearing, a Pt/Ir metal-coated AFM tip was brought into contact with the metal mask on top of the mesa (Fig. 1C). The tip apex was cold-welded to the metal by applying a force and electrical current pulse of 50 nN and 1 mA, respectively, for 1 s. As a result, a strong mechanical contact between the tip and the metal mask formed, which allowed us to apply lateral shear forces of up to 200 nN and to induce a shear glide along a single basal plane in the HOPG structure. After sliding, the exposed basal plane surface was free of observable defects,

---

IBM Research–Zürich, Säumerstasse 4, 8803 Rüschlikon, Switzerland.
*Corresponding author. E-mail: drg@zurich.ibm.com

as confirmed by AFM inspection of sheared mesas (Fig. 1E).

We measured the lateral shear force required to move the tip parallel to the mesa plane at zero applied normal force (Fig. 2). The observed force signal has several distinct features: (i) The lateral force changes sign when the tip passes from the left position through the center and then to the right position, reaching the same average plateau value of $F_P \approx 45$ nN. (ii) In the plateau regions, the lateral force is essentially independent of the scan direction and position. (iii) The measured force signal is highly reproducible throughout repeated lateral scans. From (i) and (ii), we conclude that the lateral shear force is dominantly conservative in nature; from (iii), we conclude that the sheared interface geometry is stable throughout the experiment and the manipulations are nondestructive.

Starting from the center position toward the right or left side, the lateral force builds up at a rate of ~10 nN nm^{-1} until it saturates at the plateau value F_P. In this initial phase, the upper section of the mesa, termed the mobile section, remains fixed until sufficient shear stress is built up in the mesa to trigger yielding at a glide plane. Sliding of the mobile section sets in at a tip displacement of ~5 nm, after which the tip displacement represents the actual sliding motion of the mobile section (Fig. 2B). The force trace and retrace signals exhibit substantial fluctuations and hysteresis (Fig. 2B, inset), similar to those observed in the sliding friction of carbon nanotubes (*16*) and in superlubricity sliding of nanoscale flakes (*4*) for a rotational mismatch of greater than 5° between the sliding surfaces.

Conservative displacement forces are strictly a function of the displacement x, whereas dissipative friction forces depend on the direction of motion. The overall energy dissipation for a closed path of length ℓ is given by

$$E_{\text{diss}} = \int_0^{\ell} F_{\text{fr}}\, dx \qquad (1)$$

where the friction force is given by the difference of the measured shear force at a position x between trace and retrace sliding, $F_{\text{fr}}(x) = F_{\text{S,trace}}(x) - F_{\text{S,retrace}}(x)$. An apparent correlation appears as high or low friction force values persist over sliding distances of 10 to 50 nm (Fig. 3A). We also observed unusual behavior, such as short-lived amplitude spikes (up to 10 nN) and negative friction force over some sliding paths. The latter feature indicates energy recovery during such phases.

The values of the friction force are Gaussian-distributed, with a mean value of 1.6 nN and a variance of $\sigma_{\text{fr}} = 2.45$ nN (Fig. 3C). From the central limit theorem, we conclude that the friction force arises from statistically independent events with finite correlation lengths. Therefore, we expect that the variance of the distribution of the friction force averaged over a sliding interval Δx should converge to a zero value, provided that enough independent events are probed in the sliding interval. On the other hand, correlation manifests itself as a persistence of the variance if the averaging interval Δx is smaller than the correlation length. As anticipated from the intuitive interpretation of the friction force data (Fig. 3A), the variance decays as expected for statistically independent events if the averaging interval is larger than ~20 nm (Fig. 3D). By averaging over a sliding distance of 90 nm, we obtain a robust number for the mean friction force of 1.6 nN (1σ uncertainty of 0.3 nN).

From the measured interface energy $\sigma \approx 0.227$ J m^{-2} (see below), we estimate the load force to be on the order of $P \approx (\sigma/c)(\pi r^2) \approx 24$ μN for a cylindrical mesa with a radius of $r = 100$ nm and assuming an interaction length $c \approx 0.3$ nm, on the order of the c-axis lattice spacing. From this estimated load, we obtain an effective friction coefficient of $\mu \approx 7 \times 10^{-5}$, which is more than three orders of magnitude lower than the typical friction coefficient $\mu \approx 0.1$ to 0.3 observed in dry sliding contacts.

Theoretical arguments and simulations predict that the friction force does not scale with the contact area A (*17*, *18*). The effect originates from a cancellation of forces acting on the interface atoms except at the periphery. The exponent γ in the scaling equation $F_{\text{fr}} \propto A^{\gamma}$ can assume values in the range from 0 to 0.5, depending on the type of lattice mismatch and the shape of the sliding object (*18*, *19*). Recently, fractional scaling has been confirmed in an experiment that measured the sliding friction forces of amorphous antimony and single-crystal gold islands on a graphite surface (*20*). For the amorphous islands, an exponent of $\gamma = 0.5$ was measured, as predicted by theory for a random interface. For the single-crystal Au islands, an exponent of $\gamma = 0.33 \pm 0.15$ was obtained. We find $\gamma = 0.35 \pm 0.05$, in agreement with this latter value (Fig. 3B).

The friction force can also be written as $F_{\text{fr}} = F_0 N^{\gamma}$, where F_0 is the mean force acting on an

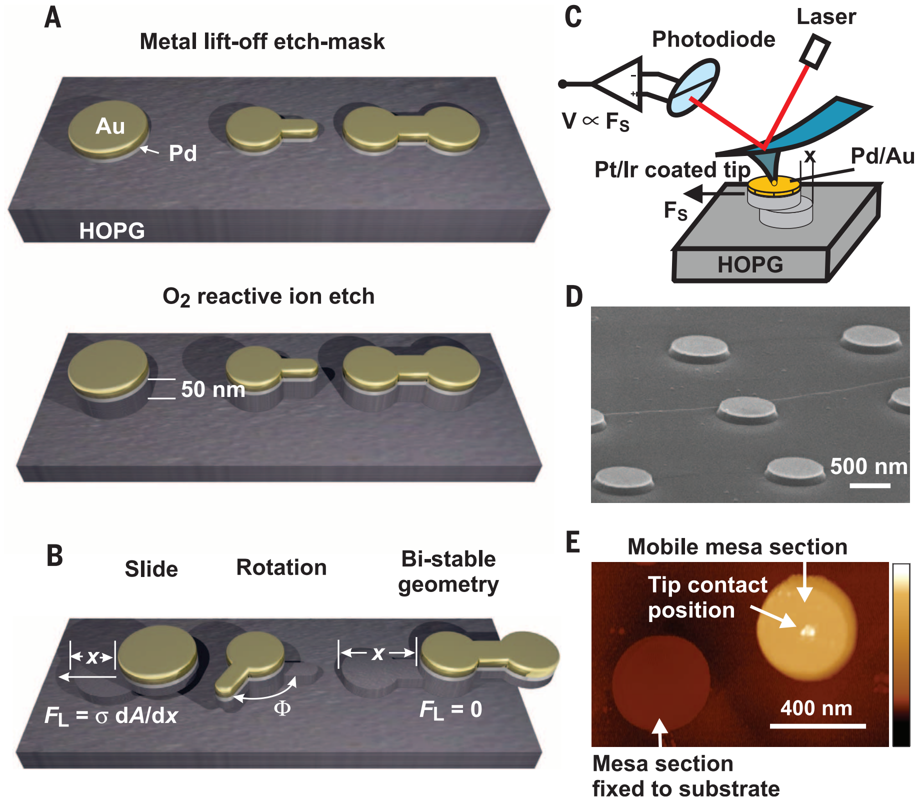

Fig. 1. Experimental procedures. (**A**) Metal masks consisting of Pd (10 nm) and Au (15 nm) are fabricated on the freshly cleaved surface of a HOPG sample by electron beam lithography and liftoff techniques. The mesa structures emerge during a dry oxygen plasma etch, which selectively thins down only the unprotected HOPG surface by 50 nm. The mesa structures are sheared along a basal glide plane by applying a corresponding force to the top metal surface. (**B**) The adhesion energy is determined by measuring the line tension force F_L acting on sheared cylindrical mesas. Stabilization of a rotation axis is possible, allowing the rotation of the mesa around the cylinder axis, while a dumbbell structure provides multiple stable equilibria whenever cylindrical sections overlap. (**C**) Schematic of the AFM experiment. A Pt/Ir tip is cold-welded to the metal mask on top of the mesas. Force is applied by a shear motion, and the shear force is measured via the induced cantilever torsion. (**D**) Scanning electron microscopy image of cylindrical mesa structures with a radius of 200 nm and etch depth of 50 nm. (**E**) AFM image of a completely sheared cylindrical mesa (100 nm height range mapped to nonlinear color scale). The mesa was sheared at a basal plane 10 nm above the substrate surface, and the top section was put down on the substrate surface to the right of the original mesa. The tip contact point close to the center is visible as a small hillock on the Au top surface.

individual atom and N is the number of interface atoms. We find $F_0 = 14^{+15}_{-8}$ pN (21) (Fig. 3B), in good agreement with the value of $F_0 \approx \sigma/(cn) \approx$ 20 pN estimated from the measured adhesion energy with an atomic density at the interface (n) of 38.2 nm^{-2}. The results suggest that the friction force originates from a genuine interaction between the rotationally misaligned graphite lattices at the sliding interface. This is remarkable because it is a well-known empirical fact (20), also predicted theoretically (17, 22), that fractional scaling is an extremely fragile interface property that can only occur if the lattice interaction is not perturbed by defects or contaminations.

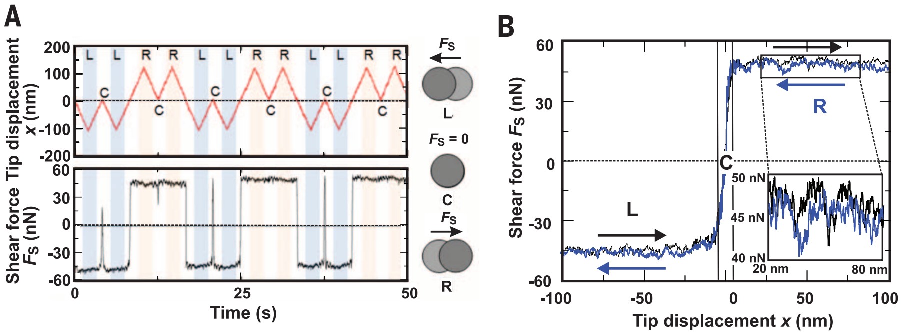

Fig. 2. Shear force measurements. (**A**) Time traces of the tip displacement x with respect to the center position (C) and the measured shear force F_S acting on the top surface of a cylindrical mesa with a radius of 100 nm. The shear force changes sign in accordance with a displacement to the right (R) or to the left (L) with respect to the center position, but not in accordance with the scan direction. (**B**) Measured shear force versus tip displacement. Black and blue curves denote the scan direction from left to right and from right to left, respectively, as indicated by the arrows. Inset: Enlarged view of the shear force for a trace and retrace scan showing the nonreversible friction contribution.

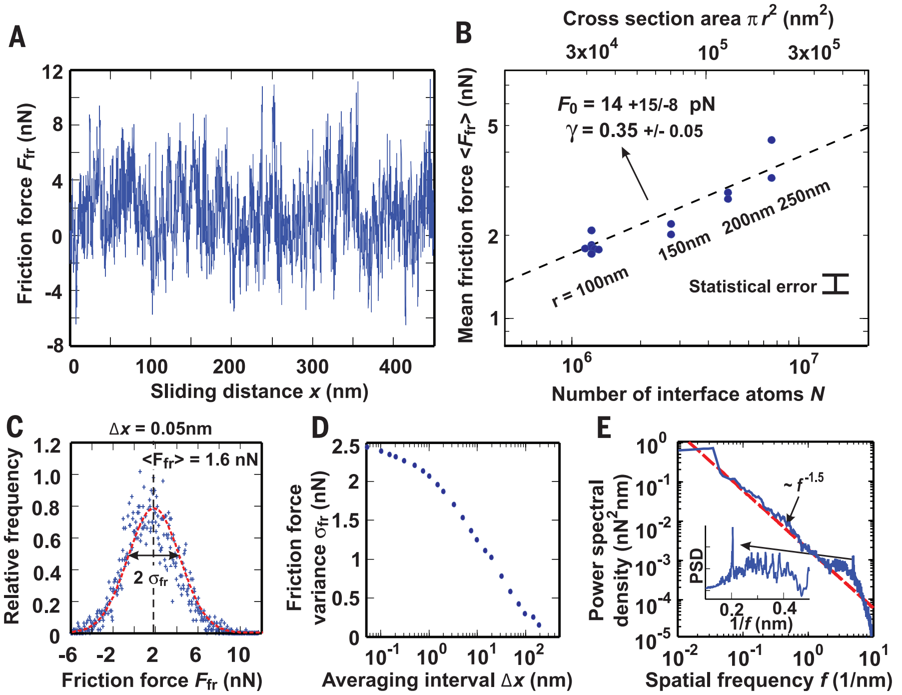

Fig. 3. Dissipative friction forces. (**A**) The friction force is defined as the difference of the shear force at a position x between trace and retrace sliding. The data represent a concatenation of five different friction force curves recorded over a sliding distance of 90 nm for mesa structures with a radius of 100 nm. (**B**) Mean value of the friction force versus cross-sectional area πr^2 or number of interface atoms N = 38.2 nm^{-2} × πr^2 determined from 90-nm trace-retrace curves of circular mesa structures with a radius r from 100 to 250 nm. Dashed line is a least-squares fit to the data with $\langle F_{fr}\rangle = F_0 N^{\gamma}$, with F_0 = 14 pN and γ = 0.35. Error bar indicates the variance $\sigma_{fr} \approx$ 0.3 nN of the data determined from (D) for Δx = 90 nm. (**C**) Histogram of the distribution of the friction force recorded at a sampling interval of Δx = 0.05 nm and a Gaussian fit (dashed line) with a mean value of $\langle F_{fr}\rangle$ = 1.6 nN and variance of σ_{fr} = 2.45 nN. (**D**) Variance σ_{fr} of the friction force distribution as a function of the averaging interval Δx. (**E**) Power spectral density (PSD) determined from the experimental friction force data shown (A). The data reveal a $f^{-1.5}$ scaling (dashed line). The inset shows the PSD as a function of period in the range from 0.1 to 0.5 nm.

Numerical simulations of adhesion interaction between two circular graphene sheets with radii of 4 to 15 nm show that a moiré superstructure, attributable to the lattice misorientation in the rotated sheets, is the root cause for the fluctuating shear forces (21). The superstructure is isomorphic to the graphene lattice and consists of domains of approximate AB and AA stacking corresponding to atomic and hollow sites in the graphene lattice, respectively. The lattice period of the superstructure is given by

$$L = \frac{a}{\sqrt{2 - 2\cos\Phi}} \tag{2}$$

where a = 0.142 nm denotes the in-plane lattice constant of graphite and Φ is the rotation angle. The moiré pattern is shifted roughly perpendicular to the slide direction by one lattice constant L for a lateral displacement of the graphene sheets by one lattice unit a. As a result, the shear force exhibits a multitude of periodic maxima and minima, with periods on the order of 0.2 to 0.4 nm, whenever stacking domains enter or leave the overlap area at the boundary (fig. S3A). According to the Tomlinson mechanism, such short-period force fluctuations are responsible for energy dissipation and friction in the system. The amplitude of the force fluctuations scales with the overlap area approximately to the power of 0.35, similar to the friction force scaling observed in the experiment, and scales with the rotation angle to the power of –1.5 (fig. S4). From the simulations we conclude that the mean rotational misalignment between the sliding surfaces in the experiment must be between 5° and 10°, which gives the correct order of magnitude of fluctuations of the shear force in relation to the experimental friction force values (fig. S4B).

In a real experiment, sliding is performed using a compliant actuator, and hence neither the rotation angle Φ nor the off-axis y position are strictly constant, which profoundly affects the sliding friction (23, 24). Allowing the top sliding surface to follow a path in the x-y-Φ space that locally minimizes the interface energy leads to a hidden pseudo–random walk trajectory in the y-Φ space and corresponding correlations. In the model simulation, we also included thermal activation by allowing the system to choose among all path energy options, with probabilities proportional to the corresponding Boltzmann factors. The surprising result of the simulation is that the character of the force fluctuations changes from a periodic pattern (fig. S3A) to a highly random spiky pattern (fig. S6A). This pattern is strikingly similar to the measured friction force (Fig. 3A). Rotational degrees of freedom have been proposed as a mechanism leading to irregular sharp peaks in the friction signal due to the restoration of a high-friction state when the sliding surfaces reorient into a commensurate state (23). In our case, however, the force spikes are not signaling a commensurate state between the sliding lattices, but rather a randomly occurring high energy barrier in the potential landscape of rotated sliding interface.

The correlations arising from the pseudo–random walk in the y-Φ space are reflected in a non-integer power law scaling with an exponent of –1.5 of the power spectral density determined from the experimental (Fig. 3E) and simulated data (fig. S6). Interestingly, the lattice structure still shows up in the power spectrum at spatial periods in the range from 0.2 to 0.5 nm with a prominent peak at 0.2 nm, corresponding to the periods obtained for a rigid slide—that is, $\Delta y = 0$ and $\Delta\Phi = 0$. The fact that we experimentally observe spectral features that can be traced back to the lattice interaction provides additional evidence that the measured friction force is genuinely due to a moiré interaction between rotated surfaces at the interface. It is also clear from the pseudo–random walk mechanism that forward and backward slides will never follow exactly the same path; this explains the huge spread of the observed local friction force, which can even assume negative values over some slide intervals.

The dominant conservative part of the lateral force is due to the interface energy at the glide planes, which gives rise to a line tension force opposing the creation of new surface area. The component of the line tension force in the slide direction is

$$F_{\mathrm{L}} = \sigma\frac{dA}{dx} \tag{3}$$

where the interface tension σ denotes the mean adhesion energy per unit area, A is the overlap area of the mesa sections, and x is the displacement of the mobile section with respect to the initial position. For a mesa with a circular cross section of radius r, we find

$$A(x) = 2r^2\left[\cos^{-1}\left(\frac{x/_2}{r}\right) - \frac{x/_2}{r}\sqrt{1-\left(\frac{x/_2}{r}\right)^2}\right] \tag{4}$$

and

$$F_{\mathrm{L}}(x) = -2\sigma r\sqrt{1-\frac{(x/_2)^2}{r^2}} \tag{5}$$

The maximum force $F_{\mathrm{S0}} = 2\sigma r$ that has to be applied to initiate sliding must be equal to the line tension force at zero displacement x. Therefore, F_{S0} scales linearly with r, as is confirmed by the experimental data (Fig. 4A). We obtain an interface tension of $\sigma = 0.227 \pm 0.005\ \mathrm{J\ m^{-2}}$ (*21*), which is ~15% larger than previously reported experimental values measured for the interaction between graphite sheets in contact (*13*, *14*). The value is in excellent agreement with the mean interface energy calculated from the model of Kolmogorov *et al.* (*9*, *21*).

To validate the interface energy picture, we measured the force characteristics for a complete slide from perfect overlap at $x = 0$ nm to zero overlap at $x = 2r$ (Fig. 4B). The measured force curves for the cylindrical mesas are perfectly predicted by Eq. 5 using our experimental value of σ. Also shown is the force curve measured for a compound mesa structure consisting of a cylindrical section with a radius of 200 nm connected to a rectangular beam section pointing along the slide direction (Fig. 4B). The first part of the force curve is identical to that of a circular structure, and for $x > 400$ nm the force is constant because of the linear decrease of the overlap area on the rectangular beam section. The slight deviation from the predicted characteristics at the crossover is due to the tapered profile in the actual device.

We observed a gradual asymptotic approach to the line tension force curves characterizing mesa sliding. This shows that the process leading to superlubricity is a continuous one, which in some cases can extend over a distance of up to 50 nm, as seen in the force trace of the large compound mesa structure (Fig. 4B). On the other hand, assuming that the graphite stack is in perfect lattice registry, we would expect that a huge breakoff force is required in order to overcome the lattice barrier. The binding energies for regular AB stacking are on the order of $E_{\mathrm{AB}} = 0.14$ to $0.34\ \mathrm{J\ m^{-2}}$, yielding a breakoff force on the order of $A \times (E_{\mathrm{AB}}/c) \approx A \times (0.5\text{ to }1.1\ \mathrm{nN\ nm^{-2}})$. For our mesa structures, this is in the range from 1 to 100 μN, which we never observed. The details of the breakoff mechanism are not clear. Initiation of the glide plane could, for example, be tied to stacking fault planes (*25*) or could involve the propagation of local stacking boundary defects (*26*). Because we see no breakoff force, we conclude that the shear strength Y_{S} for basal plane sliding in graphite mesostructures is solely governed by line tension forces, $Y_{\mathrm{S}} = F_{\mathrm{L}}/A = \sigma(d \log A/dx)$, and therefore it depends on the structure's geometry rather than being a generic material constant.

To assure the feasibility of surface force-driven actuation, we must require that the friction forces are negligible with respect to the line tension forces; that is, $\max F_{\mathrm{fr}} < F_{\mathrm{L}}$. The friction forces scale as the radius r of the structure to the power of 2γ. A safe bound for the maximum of the friction force in accounting for the substantial fluctuations is provided by a $6\sigma_{\mathrm{fr}}$ criterion, yielding an estimated maximum friction force of $\max F_{\mathrm{fr}} \approx 6\sigma_{\mathrm{fr}}(r_0)[(r/r_0)^{2\gamma}]$, where r_0 denotes the radius of a characterized reference structure. With F_{L} from Eq. 5, we obtain a lower cutoff radius of

$$r > \left(\frac{6\sigma_{\mathrm{fr}}(r_0)}{r_0^{2\gamma}}\frac{1}{2\sigma}\right)^{\frac{1}{1-2\gamma}} \tag{6}$$

Substituting the measured values from the experiment, $r_0 = 100$ nm, $\sigma_{\mathrm{fr}}(r_0) = 2.45$ nN, $\gamma = 0.35$, and $\sigma = 0.227\ \mathrm{J\ m^{-2}}$, we conclude that line tension forces dominate friction forces down to structure sizes with a radius of ~2 nm. This result is encouraging in view of the technical feasibility of graphene-based nanomechanical devices. However, structures with dimensions on the order of tens of nanometers would still be required in order to guarantee low-energy dissipation actuation in line with the low value of the mean friction force.

Determining the underlying theory to calculate intrinsic adhesion energy and forces allows us to engineer the structure geometry with respect

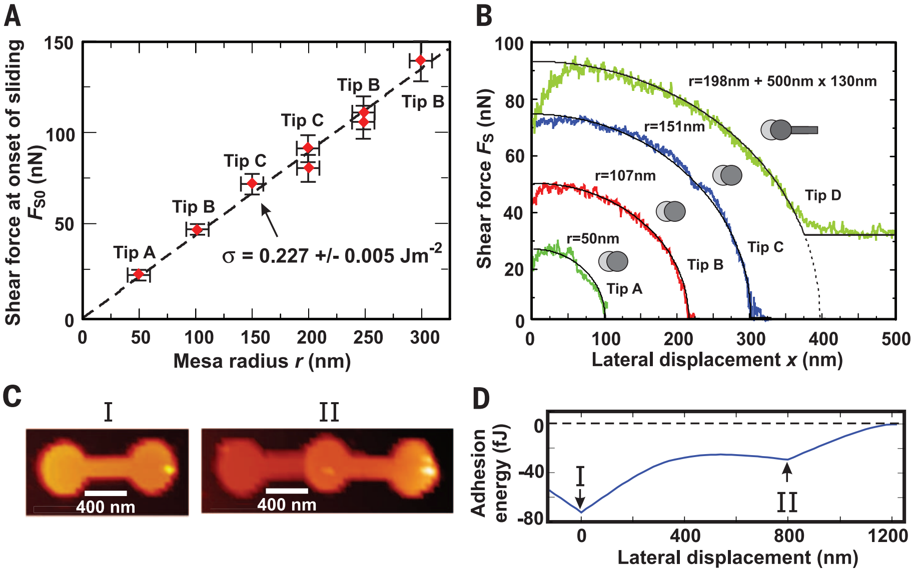

Fig. 4. Conservative forces due to adhesion energy. (**A**) Shear force at onset of mesa sliding F_{S0} as a function of the radius of cylindrical mesas. Standard deviation indicated by error crosses (*21*). Three different cantilevers (tips A, B, and C) were used. Dashed line corresponds to a weighted least-squares fit to the data, yielding $\sigma = 0.227\ \mathrm{J\ m^{-2}}$ with a variance of $0.005\ \mathrm{J\ m^{-2}}$. (**B**) Measured shear force F_{S} as a function of the lateral displacement x of the mobile top mesa section for different mesa structures and different cantilevers. Solid lines show the calculated shear force according to Eq. 5. The dotted line in the graph of the compound structure shows the extrapolation of the shear force for the cylindrical part only. (**C**) Dumbbell mesa structure with a height of 80 nm before and after sliding to a stable equilibrium position where the circular sections overlap. The glide plane is at a height of 70 nm above the substrate surface. (**D**) Calculated adhesion energy for the dumbbell mesa structure.

to a targeted energy and corresponding displacement force profile. For example, structures featuring multiple local energy minima displacement profiles act as metastable geometric traps. Switching between the trap states involves only minimal frictional resistance and virtually zero wear. The mechanical transition between local minima can be realized by different means such as mechanical, electrostatic, and magnetic actuation or by a thermal gradient mechanism (*27*). Multiple energy minima positions are obtained, for example, in a dumbbell structure (Fig. 4, C and D). The AFM tip is used to first induce a glide plane defect and then direct the mobile upper part from the initial energy minimum position (Fig. 4C, left inset) to the other local energy minimum position where the cylindrical sections overlap (Fig. 4C, right inset). After actuation, the tip is released from the metal surface by applying a negative load of >200 nN, and the actuated mesa is imaged in the tapping mode. Note that the glide plane surface of the fixed bottom mesa is clearly visible in the AFM image. Adhesion guiding combined with ultralow-friction properties can also be exploited for stabilizing rotational structures (fig. S1) and thus provides a versatile engineering platform for nanoscale devices in general.

REFERENCES AND NOTES

1. A. Vanossi, N. Manini, M. Urbakh, S. Zapperi, E. Tosatti, *Rev. Mod. Phys.* **85**, 529–552 (2013).
2. B. Bhushan, J. N. Israelachvili, U. Landman, *Nature* **374**, 607–616 (1995).
3. J.-M. Martin, C. Donnet, T. Le Mogne, T. Epicier, *Phys. Rev. B* **48**, 10583–10586 (1993).
4. M. Dienwiebel *et al.*, *Phys. Rev. Lett.* **92**, 126101 (2004).
5. X. Feng, S. Kwon, J. Y. Park, M. Salmeron, *ACS Nano* **7**, 1718–1724 (2013).
6. J. Cumings, A. Zettl, *Science* **289**, 602–604 (2000).
7. Z. Liu *et al.*, *Phys. Rev. Lett.* **108**, 205503 (2012).
8. M. Dion, H. Rydberg, E. Schröder, D. C. Langreth, B. I. Lundqvist, *Phys. Rev. Lett.* **92**, 246401 (2004).
9. A. N. Kolmogorov, V. H. Crespi, *Phys. Rev. B* **71**, 235415 (2005).
10. S. Lebègue *et al.*, *Phys. Rev. Lett.* **105**, 196401 (2010).
11. L. Spanu, S. Sorella, G. Galli, *Phys. Rev. Lett.* **103**, 196401 (2009).
12. X. Chen, F. Tian, C. Persson, W. Duan, N.-X. Chen, *Sci. Rep.* **3**, 3046 (2013).
13. L. X. Benedict *et al.*, *Chem. Phys. Lett.* **286**, 490–496 (1998).
14. Z. Liu *et al.*, *Phys. Rev. B* **85**, 205418 (2012).
15. R. Zacharia, H. Ulbricht, T. Hertel, *Phys. Rev. B* **69**, 155406 (2004).
16. A. Kis, K. Jensen, S. Aloni, W. Mickelson, A. Zettl, *Phys. Rev. Lett.* **97**, 025501 (2006).
17. M. H. Müser, L. Wenning, M. O. Robbins, *Phys. Rev. Lett.* **86**, 1295–1298 (2001).
18. A. S. de Wijn, *Phys. Rev. B* **86**, 085429 (2012).
19. E. Gnecco, E. Meyer, *Fundamentals of Friction and Wear* (Springer, New York, 2007).
20. D. Dietzel, M. Feldmann, U. D. Schwarz, H. Fuchs, A. Schirmeisen, *Phys. Rev. Lett.* **111**, 235502 (2013).
21. See supplementary materials on *Science* Online.
22. U. Tartaglino, V. N. Samoilov, B. N. Persson, *J. Phys. Condens. Matter* **18**, 4143–4160 (2006).
23. A. E. Filippov, M. Dienwiebel, J. W. M. Frenken, J. Klafter, M. Urbakh, *Phys. Rev. Lett.* **100**, 046102 (2008).
24. A. S. de Wijn, C. Fusco, A. Fasolino, *Phys. Rev. E* **81**, 046105 (2010).
25. E. Koren, A. Knoll, E. Lörtscher, U. Duerig, *Nat. Commun.* **5**, 5837 (2014).
26. P. San-Jose, R. V. Gorbachev, A. K. Geim, K. S. Novoselov, F. Guinea, *Nano Lett.* **14**, 2052–2057 (2014).
27. A. Barreiro *et al.*, *Science* **320**, 775–778 (2008).

ACKNOWLEDGMENTS

We thank U. Drechsler and M. Tschudy for invaluable technical support and M. Despont, D. Grogg, O. Hod, and R. Allenspach for stimulating discussions. Supported by the FP7 Marie Curie Actions of the European Commission and ITN fellowship cQOM (Project ID 290161) (E.K.). Data are available in the supplementary materials or upon request.

SUPPLEMENTARY MATERIALS

www.sciencemag.org/content/348/6235/679/suppl/DC1
Materials and Methods
Supplementary Text
Figs. S1 to S11
Tables S1 to S3
References (*28–41*)

3 December 2014; accepted 2 April 2015
10.1126/science.aaa4157

SOLAR CELLS

Impact of microstructure on local carrier lifetime in perovskite solar cells

Dane W. deQuilettes,[1] Sarah M. Vorpahl,[1] Samuel D. Stranks,[2]* Hirokazu Nagaoka,[1] Giles E. Eperon,[2] Mark E. Ziffer,[1] Henry J. Snaith,[2] David S. Ginger[1]†

The remarkable performance of hybrid perovskite photovoltaics is attributed to their long carrier lifetimes and high photoluminescence (PL) efficiencies. High-quality films are associated with slower PL decays, and it has been claimed that grain boundaries have a negligible impact on performance. We used confocal fluorescence microscopy correlated with scanning electron microscopy to spatially resolve the PL decay dynamics from films of nonstoichiometric organic-inorganic perovskites, $CH_3NH_3PbI_3(Cl)$. The PL intensities and lifetimes varied between different grains in the same film, even for films that exhibited long bulk lifetimes. The grain boundaries were dimmer and exhibited faster nonradiative decay. Energy-dispersive x-ray spectroscopy showed a positive correlation between chlorine concentration and regions of brighter PL, whereas PL imaging revealed that chemical treatment with pyridine could activate previously dark grains.

As active layers in solar cells, organic-inorganic perovskites (*1*, *2*) combine the promise of solution processing (*3*, *4*) with the ability to tailor the band gap through chemical substitution (*5–7*), yielding solar cell power conversion efficiencies as high as 20.1% (*8*). Concomitant with their photovoltaic performance, perovskites also exhibit high fractions of radiative recombination, with apparent carrier lifetimes of 250 ns or longer (*9*, *10*), and are challenging the dogma that solution-processed semiconductors inevitably possess high densities of performance-limiting defects. Ensuring that all recombination is radiative is critical for approaching the thermodynamic efficiency limits for solar cells and other optoelectronic devices (*11*).

Carrier recombination lifetimes measured by photoluminescence (PL) are commonly taken as a hallmark of perovskite film quality, with longer decay lifetimes used as indicators of better-performing materials (*9*, *10*, *12–14*). Carrier recombination kinetics have been described as a combination of trap-assisted, monomolecular (first-order), and bimolecular (second-order) recombination (*15*). Although most studies agree that radiative bimolecular recombination dominates at high initial carrier densities ($n_0 > 10^{17}$ cm^{-3}) (*15–18*), reports of kinetics at lower excitation densities (and relevant to solar cell operation) (*19*) range from single-exponential (*12*, *20*), to biexponential (*13*, *14*), to stretched-exponential (*6*, *9*) functions with varying levels of fidelity. These distributions have in turn been explained in terms of unintentional doping (*21*) or charge trapping (*22*). The perovskite growth conditions (*3*, *4*, *10*) and post-deposition treatments (*12*, *23*) can greatly alter film morphology, carrier lifetime, and device performance, yet the underlying relations between these parameters are important open questions. For instance, perovskite films grown from nonstoichiometric mixed halide (Cl/I) precursor solutions have exhibited lifetimes of hundreds of nanoseconds, but PL lifetimes in films grown from chloride-free precursors are generally much shorter (*9*, *20*).

Correlated confocal PL and scanning electron microscopy (SEM) have been a powerful tool to reveal structure/function relationships in biology (*24*). We applied similar techniques to study structure/function relationships in perovskite films. We found substantial local PL heterogeneity even for $CH_3NH_3PbI_3(Cl)$ films with average lifetimes of ~1 μs (comparable to the longest lifetimes reported) (*9*, *10*), which suggests that considerable

---

[1] Department of Chemistry, University of Washington, Box 351700, Seattle, WA 98195-1700, USA. [2] Clarendon Laboratory, University of Oxford, Parks Road, Oxford OX1 3PU, UK.
*Present address: Research Laboratory of Electronics, Massachusetts Institute of Technology, Cambridge, MA 02139, USA. **†Corresponding author. E-mail: ginger@chem.washington.edu**

EXTENDED PDF FORMAT
SPONSORED BY
Sample-Size Antibodies
Now Available
Learn More
R&D SYSTEMS
a biotechne brand
www.rndsystems.com

Adhesion and friction in mesoscopic graphite contacts

Elad Koren *et al.*

Science **348**, 679 (2015);
DOI: 10.1126/science.aaa4157

This copy is for your personal, non-commercial use only.

If you wish to distribute this article to others, you can order high-quality copies for your colleagues, clients, or customers by clicking here.

Permission to republish or repurpose articles or portions of articles can be obtained by following the guidelines here.

The following resources related to this article are available online at www.sciencemag.org (this information is current as of April 8, 2016):

Updated information and services, including high-resolution figures, can be found in the online version of this article at:
/content/348/6235/679.full.html

Supporting Online Material can be found at:
/content/suppl/2015/05/06/348.6235.679.DC1.html

A list of selected additional articles on the Science Web sites **related to this article** can be found at:
/content/348/6235/679.full.html#related

This article **cites 36 articles**, 3 of which can be accessed free:
/content/348/6235/679.full.html#ref-list-1

This article has been **cited by** 2 articles hosted by HighWire Press; see:
/content/348/6235/679.full.html#related-urls

This article appears in the following **subject collections:**
Materials Science
/cgi/collection/mat_sci

Downloaded from on April 8, 2016

Science (print ISSN 0036-8075; online ISSN 1095-9203) is published weekly, except the last week in December, by the American Association for the Advancement of Science, 1200 New York Avenue NW, Washington, DC 20005. Copyright 2015 by the American Association for the Advancement of Science; all rights reserved. The title *Science* is a registered trademark of AAAS.